PERGAMON

International Journal of Solids and Structures 37 (2000) 7329–7348

INTERNATIONAL JOURNAL OF SOLIDS and STRUCTURES

www.elsevier.com/locate/ijsolstr

Formulation of an implicit algorithm for finite deformation viscoplasticity

W.M. Wang [a], L.J. Sluys [b,*]

[a] *Crash Safety Centre, TNO Automotive, P.O. Box 6033, 2600 JA Delft, Netherlands*

[b] *Faculty of Civil Engineering and Geosciences, Delft University of Technology, P.O. Box 5048, 2600 GA Delft, Netherlands*

Received 22 September 1999; in revised form 14 February 2000

Abstract

Within the framework of additive plasticity, an objective stress update algorithm has been proposed. The procedure is implemented in such way that the extension from a standard small strain FE code to the finite strain range is straightforward, and objectivity can be retained for any choice of the intermediate configuration. The additional computational cost only includes some geometrical manipulations. For the Newton–Raphson iteration method, a closed-form solution of the consistent tangent is derived by direct linearization of the stress update algorithm. Numerical examples show a quadratic rate of convergence with the proposed viscoplastic model. The analysis of a tensile test first shows a shear band with a finite thickness independent of the finite element size. At large deformation, the shear band pattern transforms into a necking failure mode. As a second example, a thin sheet tensile test is analyzed. A necking failure mode leads to global softening even though, locally, the material is still hardening. Although viscoplastic regularization is used, the results still show a mesh dependence for deformations over 40%.

Keywords: Implicit algorithm; Finite deformation viscoplasticity

1. Introduction

Numerical modeling of finite strain plasticity problems involves two basic types of nonlinearity: material nonlinearity (plastic behavior) and geometrical nonlinearity (finite strain). Nonlinear material behavior is often described by a rate-form constitutive equation, relating the rate of stress to the rate of strain and some internal variables (Malvern, 1969). If geometrical nonlinearity is considered, the choice of proper stress and strain rates is crucial, because the principle of objectivity should be respected; the constitutive equation must be independent of the observer. This is only achieved when objective tensor quantities are employed. A large body of literature has been concerned with the development of objective rates which, remarkably,

* Corresponding author. Tel.: +31-15-278-2728; fax: +31-15-2786383.
E-mail address: l.j.sluys@ct.tudelft.nl (L.J. Sluys).

0020-7683/00/$ - see front matter
PII: S0020-7683(00)00201-8

extends to recent dates (Simo and Marsden, 1984). The basic idea is that rigid body rotations induce no straining of a material, and this fact must be properly captured by the stress rate, which leads to the so-called *incremental objectivity* or *material frame indifference*.

Several stress update algorithms can be found in literature (Simo and Marsden, 1984; Simo and Ortiz, 1985; Cuitino and Ortiz, 1992; Rodriguez-Ferran et al., 1997). Conceptually, the formulation of an incrementally objective algorithm proceeds as follows. The given (objective) spatial rate constitutive equation is mapped to an intermediate configuration, which is unaffected by superposed spatial rigid body motions. A time-stepping algorithm is then performed in this local configuration and the discrete equation is mapped back to the Eulerian description. In the actual implementation of this idea, two basic methodologies can be adopted:

(1) The convective or material representation (Simo and Ortiz, 1985; Cuitino and Ortiz, 1992; Rodriguez-Ferran et al., 1997) – in this approach, one exploits the fact that objects in the convective representation remain unaltered under supposed spatial rigid body motion. Therefore, an objective algorithm can be obtained by appropriate tensorial transformation of the objects between spatial and material representation. Equivalently, by using convected coordinates, the equations automatically satisfy the objectivity requirement.

(2) The local rotated representation (Simo and Marsden, 1984) – in this approach, the evolution equation is transformed to a locally cartesian rotating coordinate system, which is constructed precisely as to ensure that the rotated objects (the Jaumann derivative) remain unaltered under superposed spatial rigid body motion. The stress update is then performed in the rotated description, and the discrete equation is subsequently transformed back to the spatial configuration.

The crucial computational aspect in the second methodology is the determination of the rotated local configuration. As pointed out by Hughes (1983), the problem can be reduced to the numerical integration of an initial value problem that generates a one-parameter subgroup of proper orthogonal transformations. However, a closed form linearization of the algorithm remains an open question, and therefore, the formulation of a consistent tangent operator cannot be successful. In this paper, the convective representation will be adopted to develop a large-strain finite element (FE) code, because it leads to a simplification of the numerical time integration of the constitutive equation and yields a closed-form solution of the consistent tangent operator. This is the new contribution of this paper. The procedure is implemented in such way that the extension from a standard small strain FE code to the finite strain range is straightforward, and objectivity can be retained for any choice of the intermediate configuration. The additional computational cost only includes some geometrical manipulations.

The paper is organized as follows: In Section 2, the necessary continuum mechanical notions needed for the description of the stress update algorithm in Section 3 are given. In Section 4, the consistent tangent is derived for a finite strain viscoplasticity modeling. In Section 5, a stretch test is described in which small deformations show shear bands of finite thickness, which is set up by the viscous length scale parameter, and large deformations demonstrate a transition from shear banding to necking. A thin sheet tensile test is analyzed to further explore the necking failure mode. Although viscoplastic regularization is used, mesh dependence is still observed for very large deformations.

2. Kinematics

In standard nonlinear solid mechanics, two coordinate systems are adopted (Fig. 1). To identify a material particle, a material or convected coordinate X^I is introduced. Further to describe the motion of a material point, a spatial coordinate y^i is needed. If we consider a material particle P which occupies position $\mathbf{Y} = \mathbf{Y}(P, 0)$ in space at the undeformed state, then, at the current time this material point will be denoted by a spatial vector $\mathbf{y} = \mathbf{y}(p, t)$. Note that we will use upper case letters to denote material quantities as-

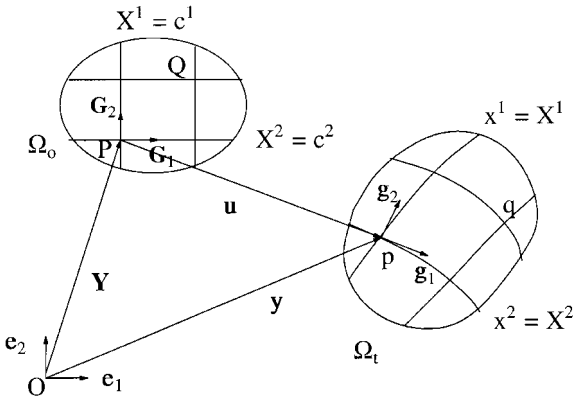

Fig. 1. Coordinate systems and base vectors.

sociated with the undeformed configuration and lower case letters for the deformed configuration. For example, the material line element PQ (Fig. 1) in the current time can be written as

$$\mathrm{d}\mathbf{y}(t) = \mathrm{d}y^i(t)\mathbf{e}_i. \tag{1}$$

Eq. (1) is described in the spatial coordinate system with an orthonormal base vector $\mathbf{e}_i$. Alternatively, the material line element can be written in the material coordinate system as

$$\mathrm{d}\mathbf{x}(t) = \mathrm{d}x^i\mathbf{g}_i(t) \tag{2}$$

with the deformed local covariant base vector

$$\mathbf{g}_i(t) = \frac{\partial \mathbf{y}(t)}{\partial x^i} = \frac{\partial y^j(t)}{\partial x^i}\mathbf{e}_j = \frac{\partial y^j(t)}{\partial Y^I}\mathbf{e}_j, \tag{3}$$

where we choose the material coordinate identical to the spatial coordinate at the initial state $x^i = X^I = Y^I$. Note that in general, the material base vector $\mathbf{g}_i$ is not orthonormal. For convenience of tensor algebra in the material description, the respective contravariant base vector $\mathbf{g}^i$ is frequently used, i.e.

$$\mathbf{g}^i \cdot \mathbf{g}_j = \delta^i_j, \tag{4}$$

where δ is the Kronecker delta. The covariant and contravariant base vectors can be mapped to each other as

$$\mathbf{g}_i = g_{ij}\mathbf{g}^j \quad \text{and} \quad \mathbf{g}^i = g^{ij}\mathbf{g}_j \tag{5}$$

by the covariant and contravariant components of the metric tensor

$$\mathbf{g} = \mathbf{g}_i \otimes \mathbf{g}^i = \mathbf{g}^i \otimes \mathbf{g}_i = g_{ij}\mathbf{g}^i \otimes \mathbf{g}^j = g^{ij}\mathbf{g}_i \otimes \mathbf{g}_j. \tag{6}$$

If we introduce the so-called deformation gradient tensor

$$\mathbf{F} = \mathbf{g}_i \otimes \mathbf{G}^I = \frac{\partial y^i}{\partial Y^J}\mathbf{e}_i \otimes \mathbf{e}_J, \tag{7}$$

one can obtain the following relationship:

$$\mathbf{g}_i = \mathbf{F} \cdot \mathbf{G}_I, \tag{8}$$

which maps the initial material base vector ($\mathbf{G}_I = \mathbf{g}_i(0)$) onto the current material base vector, or alternatively,

$$\mathrm{d}\mathbf{y} = \mathbf{F} \cdot \mathrm{d}\mathbf{Y} \tag{9}$$

translates a material line element at the reference time to the current location, respectively.

Note that in the spatial description (1), the base vector $\mathbf{e}_i$ is constant and the components $y^i = y^i(t)$ vary during the deformation process. In the material description (2), on the other hand, the components x^i remain constant (invariant) and the material base vector $\mathbf{g}_i = \mathbf{g}_i(t)$ records the geometrical and kinematic aspects.

The convected coordinates allow strain to be defined in a general way, which will naturally lead to the familiar strain tensors. The strain tensor is defined such that when it operates on a material line element, it represents a measure of the deformation of its arc length,

$$\mathrm{d}l^2 - \mathrm{d}L^2 = \mathrm{d}\mathbf{x} \cdot \mathrm{d}\mathbf{x} - \mathrm{d}\mathbf{X} \cdot \mathrm{d}\mathbf{X} = g_{ij}\,\mathrm{d}x^i \mathrm{d}x^j - G_{IJ}\,\mathrm{d}X^I \mathrm{d}X^J. \tag{10}$$

The Lagrangian strain tensor $\mathbf{E}$ and the Eulerian strain tensor $\boldsymbol{\varepsilon}$ are defined by

$$\mathbf{E} = \tfrac{1}{2}[g_{ij} - G_{IJ}]\mathbf{G}^I \otimes \mathbf{G}^J, \tag{11}$$

$$\boldsymbol{\varepsilon} = \tfrac{1}{2}[g_{ij} - G_{IJ}]\mathbf{g}^i \otimes \mathbf{g}^j \tag{12}$$

with respect to the undeformed and deformed configurations, respectively. With $\mathbf{E}$ operating on $\mathrm{d}\mathbf{X}$ and $\boldsymbol{\varepsilon}$ operating on $\mathrm{d}\mathbf{x}$, leads to the measure of the change of arc length (10).

By analogy with the strain tensor, the strain-rate tensor can be defined such that when it operates on the corresponding line element, it gives the rate of deformation

$$\frac{\mathrm{d}}{\mathrm{d}t}\left[\tfrac{1}{2}(\mathrm{d}l^2 - \mathrm{d}L^2)\right] = \tfrac{1}{2}\dot{g}_{ij}\,\mathrm{d}x^i \mathrm{d}x^j. \tag{13}$$

Note that $\mathrm{d}x^i$ are convected, $\mathrm{d}L$ and G_{ij} are constant during the deformation process. The Lagrangian and the (objective) Eulerlain strain-rate tensors (commonly called as the rate of deformation tensor) are defined by

$$\dot{\mathbf{E}} = \tfrac{1}{2}\dot{g}_{ij}\mathbf{G}^I \otimes \mathbf{G}^J, \tag{14}$$

$$\mathring{\boldsymbol{\varepsilon}} = \tfrac{1}{2}\dot{g}_{ij}\mathbf{g}^i \otimes \mathbf{g}^j, \tag{15}$$

respectively, so that when they operate on different configurations, the result is the same quantity of Eq. (13). Note that $\dot{\mathbf{E}}$ is the material time derivative of $\mathbf{E}$, but $\mathring{\boldsymbol{\varepsilon}}$ is not the material time derivative of $\boldsymbol{\varepsilon}$ since $\dot{\mathbf{g}}^i \neq 0$.

It should be emphasized that the definition of strain rates must satisfy the so-called material frame indifference, so that a rigid body motion will not induce straining of the material. Recall that in the convected description, the material base vectors reflect the geometrical and kinematic aspects, and the corresponding components are constant with respect to their material base vectors. Therefore, in the convected frames, we can ignore the base vectors while processing the tensor algebra with the components and restoring the tensor quantity with respect to the corresponding material base vectors (Rodriguez-Ferran et al., 1997). For example, giving the Kirchhoff stress tensor

$$\boldsymbol{\tau} = \tau^{ij}\mathbf{g}_i \otimes \mathbf{g}_j \tag{16}$$

in the convected expression, one can immediately build up its objective rate

$$\mathring{\boldsymbol{\tau}} = \dot{\tau}^{ij}\mathbf{g}_i \otimes \mathbf{g}_j \tag{17}$$

by ignoring the base vectors in the time derivative. Similarly, by applying the inverse process, one obtains

$$\int_0^t \mathring{\boldsymbol{\tau}}\,\mathrm{d}t = \left[\int_0^t \dot{\tau}^{ij}\,\mathrm{d}t\right]\mathbf{g}_i \otimes \mathbf{g}_j = [\tau^{ij}(t) - \tau^{ij}(0)]\mathbf{g}_i \otimes \mathbf{g}_j = \boldsymbol{\tau}(t), \tag{18}$$

where the undeformed state is assumed stress free. A large body of literature has been concerned with the development of objective stress rates. However, one can show that any possible choice is a particular case of the Kirchhoff stress rate defined in Eq. (17).

3. Finite strain elasto-viscoplasticity

3.1. Constitutive equations

In nonlinear solid mechanics, the material behavior is often described by a rate-form (incremental) constitutive equation. The particular case of hypoelastic materials, where the stress rate (stress incremental) depends linearly on the elastic Eulerian strain-rate tensor (or the rate of deformation tensor) is used here via

$$\mathring{\boldsymbol{\tau}} = \mathbf{a} : (\mathring{\boldsymbol{\varepsilon}} - \mathring{\boldsymbol{\varepsilon}}^{\mathrm{p}}) = \mathbf{c} : \mathring{\boldsymbol{\varepsilon}}, \tag{19}$$

where $\mathbf{a}$, $\mathbf{c}$ are the elastic and elasto-plastic moduli, respectively. Furthermore, the additive decomposition of elastic and plastic parts of the Eulerian strain rate is assumed, i.e.

$$\mathring{\boldsymbol{\varepsilon}} = \mathring{\boldsymbol{\varepsilon}}^{\mathrm{e}} + \mathring{\boldsymbol{\varepsilon}}^{\mathrm{p}}. \tag{20}$$

Note that Eq. (19), in general, is not derivable from a stored energy function which leads to the so-called *hyperelastic* formulation. However, the advantage of the *hypoelastic* model relies on the conceptual simplicity of its formulation. Furthermore, for most problems in metal plasticity, the elastic strain is small with respect to the plastic deformation; therefore, the difference in the formulation of the elastic response has little or no effect on the numerical simulation. It should be stated that using hypoplasticity in a rate form has the effect that classical hyperelasticity is not recovered for zero plastic flow.

Similar to small strain plasticity, the plastic flow can be expressed as

$$\mathring{\boldsymbol{\varepsilon}}^{\mathrm{p}} = \dot{\lambda}\mathbf{n}, \quad \mathbf{n} = \frac{\partial \phi}{\partial \boldsymbol{\tau}}, \tag{21}$$

where λ is the plastic multiplier and $\mathbf{n}$ the direction of the plastic flow, which is the gradient of the plastic potential function ϕ. To determine the plastic multiplier, the loading–unloading conditions should be imposed in a Kuhn–Tucker form as

$$\dot{\lambda} \geqslant 0, \quad \Phi \leqslant 0, \quad \dot{\lambda}\Phi = 0, \quad \dot{\lambda}\dot{\Phi} = 0, \tag{22}$$

where a rate dependent yield function $\Phi = \Phi(\boldsymbol{\tau}, \boldsymbol{\kappa}, \mathring{\boldsymbol{\kappa}})$ is introduced with a number of internal variables, collected in a vector $\boldsymbol{\kappa}$, which describe the plastic deformation history. It should be mentioned that in this so-called consistency model (Wang et al., 1997), the stress remains on the yield surface, which is different from the well known overstress laws such as Perzyna and Duvaut–Lions. The consistency model, in comparison with the overstress models, has the advantage that it can be easily implemented in the classical rate-independent plasticity (Wang et al., 1997). For simplicity and without loss of generality, we consider an isotropic hardening/softening problem, where the vector $\boldsymbol{\kappa}$ reduces to a scalar quantity, the so-called equivalent plastic strain κ, which can be specified as

$$\kappa = \int_0^t \dot{\kappa}\,\mathrm{d}t, \qquad \dot{\kappa} = \sqrt{\tfrac{2}{3}\mathring{\boldsymbol{\varepsilon}}^{\mathrm{p}} : \mathring{\boldsymbol{\varepsilon}}^{\mathrm{p}}}. \tag{23}$$

3.2. Objective integration algorithms

To obtain a framework suitable for the application of a displacement based FE method at finite strain, the rate of constitutive equation should be integrated. From a computational point of view, the essential requirement for integration of Eq. (19) is the principle of material frame indifference. From a physical point of view, it requires no strain and stress of a material upon rigid body motion. Recall that in the material description, all quantities automatically satisfy the objectivity requirement, because the base vectors record the geometrical and kinematic aspects. However, because the base vectors are not orthonormal, the recorded data of experiments and also the implementation of the FE code are normally based on the cartesian reference frame. Furthermore, the current (deformed) configuration itself is unknown in the problem. It is convenient to refer all quantities to a known reference configuration, cf. the undeformed configuration. Therefore, the formulation of incrementally objective algorithms proceeds as follows (Fig. 2):

(1) *Pull back* the Kirchhoff stress rate $\mathring{\boldsymbol{\tau}}$ onto the second Kirchhoff stress rate

$$\dot{\mathbf{S}} = \mathbf{F}^{-1} \cdot \mathring{\boldsymbol{\tau}} \cdot \mathbf{F}^{-\mathrm{T}}. \tag{24}$$

(2) Apply the generalized mid-point rule for an approximation of the rates

$$\mathbf{S} - \mathbf{S}_n = \dot{\mathbf{S}}_{n+\theta}\Delta t. \tag{25}$$

(3) *Push forward* the integrated results to the current configuration by using relations

$$\mathbf{S} - \mathbf{S}_n = \mathbf{F}^{-1} \cdot \boldsymbol{\tau} \cdot \mathbf{F}^{-\mathrm{T}} - \mathbf{F}_n^{-1} \cdot \boldsymbol{\tau}_n \cdot \mathbf{F}_n^{-\mathrm{T}}. \tag{26}$$

Accordingly, the integration of Eq. (19) follows as

$$\int_n^{n+1} \mathring{\boldsymbol{\tau}}\,\mathrm{d}t = \int_n^{n+1} \mathbf{F} \cdot \dot{\mathbf{S}} \cdot \mathbf{F}^{\mathrm{T}}\,\mathrm{d}t = \mathbf{F}_{n+\theta} \cdot (\dot{\mathbf{S}}_{n+\theta}\Delta t) \cdot \mathbf{F}_{n+\theta}^{\mathrm{T}} = \mathbf{F}_{n+\theta} \cdot (\mathbf{S} - \mathbf{S}_n) \cdot \mathbf{F}_{n+\theta}^{\mathrm{T}}. \tag{27}$$

By introducing the relative deformation gradients (Fig. 3),

$$\mathbf{f}_{n+\theta} = \mathbf{F}_{n+\theta} \cdot \mathbf{F}_n^{-1}, \tag{28}$$

$$\mathbf{g} = \mathbf{F} \cdot \mathbf{F}_{n+\theta}^{-1}, \tag{29}$$

one obtains

$$\int_n^{n+1} \mathring{\boldsymbol{\tau}}\ \mathrm{d}t = \mathbf{g}^{-1} \cdot \boldsymbol{\tau} \cdot \mathbf{g}^{-\mathrm{T}} - \mathbf{f}_{n+\theta} \cdot \boldsymbol{\tau}_n \cdot \mathbf{f}_{n+\theta}^{\mathrm{T}}, \tag{30}$$

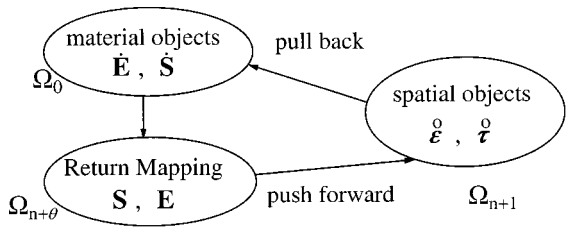

Fig. 2. The algorithm of an incrementally objective formulation.

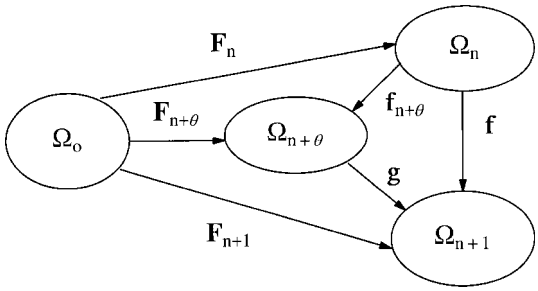

Fig. 3. Configurations and the corresponding deformation gradients.

where geometrically, $\mathbf{f}_{n+\theta}$ can be interpreted as a push-forward of the stress of Ω_n onto $\Omega_{n+\theta}$ and $\mathbf{g}$ a push-forward of the stress of $\Omega_{n+\theta}$ onto Ω_{n+1}, respectively.

Similarly, the integration of the Eulerian strain rate yields

$$\int_n^{n+1} \mathring{\boldsymbol{\varepsilon}}\, \mathrm{d}t = \int_n^{n+1} \mathbf{F}^{-\mathrm{T}} \cdot \dot{\mathbf{E}} \cdot \mathbf{F}^{-1}\, \mathrm{d}t = \mathbf{F}_{n+\theta}^{-\mathrm{T}} \cdot [\dot{\mathbf{E}}_{n+\theta} \Delta t] \cdot \mathbf{F}_{n+\theta}^{-1} = \mathbf{F}_{n+\theta}^{-\mathrm{T}} \cdot [\mathbf{E} - \mathbf{E}_n] \cdot \mathbf{F}_{n+\theta}^{-1}. \tag{31}$$

By definition of a relative (incremental) Eulerian strain,

$$\mathbf{e} = \tfrac{1}{2}\left[\mathbf{I} - (\mathbf{f}_{n+1} \cdot \mathbf{f}_{n+1}^{\mathrm{T}})^{-1}\right], \tag{32}$$

where $\mathbf{I}$ is the identity tensor, we have

$$\int_n^{n+1} \mathring{\boldsymbol{\varepsilon}}\, \mathrm{d}t = \mathbf{g}^{\mathrm{T}} \cdot \mathbf{e} \cdot \mathbf{g} = \hat{\mathbf{e}}_{n+\theta}. \tag{33}$$

With the approximation of Eqs. (30) and (33) at hand, the integration of Eq. (19) follows

$$\boldsymbol{\tau} - \mathbf{f}_{n+1} \cdot \boldsymbol{\tau}_n \cdot \mathbf{f}_{n+1}^{\mathrm{T}} = \mathbf{g} \cdot [\mathbf{c}_{n+\theta} : \mathbf{g}^{\mathrm{T}} \cdot \mathbf{e} \cdot \mathbf{g}] \cdot \mathbf{g}^{\mathrm{T}}. \tag{34}$$

If the incremental motion is rigid, then $\mathbf{f}_{n+1}$ is the rotation tensor and $\mathbf{e}$ vanishes because $\mathbf{f}_{n+1} \cdot \mathbf{f}_{n+1}^{\mathrm{T}} = \mathbf{f}_{n+1} \cdot \mathbf{f}_{n+1}^{-1} = \mathbf{I}$. Therefore, we end up with $\boldsymbol{\tau} = \mathbf{f}_{n+1} \cdot \boldsymbol{\tau}_n \cdot \mathbf{f}_{n+1}^{\mathrm{T}}$, which is the requirement of the incremental objectivity (Malvern, 1969). Note that objectivity of the integration over an interval $[t_n, t_{n+1}]$ can be retained for any choice of the intermediate configuration $\Omega_{n+\theta}$ with $\theta \in [0, 1]$, not necessarily restricted to the mid-point rule with $\theta = \frac{1}{2}$. In fact, the stability and accuracy of the return mapping algorithm is dependent on the adjustable interpolation parameter θ and the numerical examples in Sections 5.1 and 5.2 demonstrate that a larger value of θ leads to a faster convergence.

3.3. Return mapping algorithm

Assuming that the components of the elastic moduli in the cartesian coordinate are constant, one can then exclude the elastic moduli from integration. Again, by evaluating Eq. (19) at the $\Omega_{n+\theta}$ one obtains

$$\hat{\boldsymbol{\tau}}_{n+\theta} = \mathbf{g}^{-1} \cdot \boldsymbol{\tau} \cdot \mathbf{g}^{-\mathrm{T}} = \hat{\boldsymbol{\tau}}_{n+\theta}^{\mathrm{tr}} - \Delta\lambda_{n+\theta} \mathbf{a}_{n+\theta} : \mathbf{n}_{n+\theta}, \tag{35}$$

where the trial stress (assuming not yielding)

$$\hat{\boldsymbol{\tau}}_{n+\theta}^{\mathrm{tr}} = \mathbf{f}_{n+\theta} \cdot \boldsymbol{\tau}_n \cdot \mathbf{f}_{n+\theta}^{\mathrm{T}} + \mathbf{a}_{n+\theta} : \hat{\mathbf{e}}_{n+\theta} \tag{36}$$

is introduced. Note that plastic flow is approximated on $\Omega_{n+\theta}$ by means of

$$\Delta\lambda_{n+\theta} = \dot{\lambda}_{n+\theta}\Delta t, \tag{37}$$

which is consistent with the integration of strain and stress rates. To determine the incremental plastic multiplier $\Delta\lambda_{n+\theta}$, the yield function and the plastic flow direction should be specified. In general, they may depend on the specified material and the interesting range of the strain. For most problems in metal plasticity, it is popular to use a J_2 flow theory, in which the von Mises yield function and the associative plastic flow are given by

$$\phi = \Phi = \sqrt{3J_2} - \bar{\sigma}(\lambda, \dot{\lambda}), \tag{38}$$

where following standard notation, J_2 is the second invariant of the deviatoric stress $\mathbf{s}$, i.e.

$$J_2 = \tfrac{1}{2}\mathbf{s} : \mathbf{s} = \tfrac{1}{2}|\mathbf{s}|^2, \qquad \mathbf{s} = \boldsymbol{\tau} - \tfrac{1}{3}\mathrm{tr}(\boldsymbol{\tau})\mathbf{I} \tag{39}$$

and $\bar{\sigma}$ is the yielding stress which is a function of the plastic multiplier and its rate. The direction of the plastic flow (Eq. (21)) can be expressed as

$$\mathbf{n} = \frac{\partial\phi}{\partial\boldsymbol{\tau}} = \frac{\partial\phi}{\partial J_2}\left(\frac{\partial J_2}{\partial\mathbf{s}} : \frac{\partial\mathbf{s}}{\partial\boldsymbol{\tau}}\right) = \frac{3}{2\sqrt{3J_2}}(\mathbf{s}) = \sqrt{\frac{3}{2}}\frac{\mathbf{s}}{|\mathbf{s}|}, \tag{40}$$

which only includes the deviatoric part of $\boldsymbol{\tau}$. By using the relationship [1]

$$\mathbf{r} = \mathbf{n} : \mathbf{a} = \mathbf{a} : \mathbf{n} = 2\mu\mathbf{n} = 2\mu\mathbf{n}^{\mathrm{tr}}_{n+\theta} \tag{41}$$

Eq. (35) leads to

$$\hat{\boldsymbol{\tau}}_{n+\theta} = \hat{\boldsymbol{\tau}}^{\mathrm{tr}}_{n+\theta} - 2\mu\Delta\lambda_{n+\theta}\mathbf{n}^{\mathrm{tr}}_{n+\theta}, \tag{42}$$

or in the deviatoric expression

$$\hat{\mathbf{s}}_{n+\theta} = \hat{\mathbf{s}}^{\mathrm{tr}}_{n+\theta} - 2\mu\Delta\lambda_{n+\theta}\mathbf{n}^{\mathrm{tr}}_{n+\theta} = \left[1 - 2\mu\Delta\lambda_{n+\theta}\sqrt{\tfrac{3}{2}}|\hat{\mathbf{s}}^{\mathrm{tr}}_{n+\theta}|^{-1}\right]\hat{\mathbf{s}}^{\mathrm{tr}}_{n+\theta}. \tag{43}$$

Accordingly, the yield function at $\Omega_{n+\theta}$ yields

$$\phi_{n+\theta} = \sqrt{\frac{3}{2}}|\hat{\mathbf{s}}_{n+\theta}| - \bar{\sigma}_{n+\theta} = \sqrt{\frac{3}{2}}|\hat{\mathbf{s}}^{\mathrm{tr}}_{n+\theta}| - 3\mu\Delta\lambda_{n+\theta} - \bar{\sigma}_{n+\theta} = 0. \tag{44}$$

In a discrete form, Eq. (44) leads to

$$\phi^{(i+1)}_{n+\theta} = \phi^{(i)}_{n+\theta} + \mathbf{n}^{\mathrm{tr}}_{n+\theta} : \delta\hat{\boldsymbol{\tau}}^{\mathrm{tr}}_{n+\theta} - 3\mu\delta\lambda_{n+\theta} - h^{(i)}\delta\lambda_{n+\theta} = 0. \tag{45}$$

Therefore, the iterative incremental plastic multiplier reads

$$\delta\lambda_{n+\theta} = \frac{1}{3\mu + h^{(i)}}\left[\phi^{(i)}_{n+\theta} + \mathbf{n}^{\mathrm{tr}}_{n+\theta} : \delta\hat{\boldsymbol{\tau}}^{\mathrm{tr}}_{n+\theta}\right], \tag{46}$$

where the effective softening/hardening parameter $h^{(i)}$ reads

$$h^{(i)}_{n+\theta} = \left[\frac{\partial\bar{\sigma}}{\partial\lambda} + \frac{1}{\Delta t}\frac{\partial\bar{\sigma}}{\partial\dot{\lambda}}\right]^{(i)}_{n+\theta}. \tag{47}$$

[1] Note that $\mathbf{n}$ is the covariant tensor $\mathbf{r}$ is the contravariant tensor. For von Mises associative flow, the plastic flow direction is determined by the trial stress.

If we use local iterations during a global iteration, the iterative incremental stress $\delta\hat{\boldsymbol{\tau}}^{\mathrm{tr}}_{n+\theta}$ vanishes from Eq. (46). In Appendix A.1 the stress update algorithm for J_2 flow theory is outlined.

Note that the stress is updated in a straightforward manner using the standard return mapping algorithm in a small strain FE code. The additional computational cost for a extension to a finite strain FE code only includes some geometrical manipulations (cf. push forward and pull back).

4. The consistent tangent

In an implicit displacement based FE formulation, equilibrium in a time step can be obtained by means of the Newton–Raphson method, which linearizes the nonlinear equilibrium equation at each iteration and yields the so-called *consistent tangent*. Such a consistent tangent plays a crucial role in reducing the computation time. In this section, we will outline the consistent linearization of the discretized momentum balance equation and show that the return mapping algorithm discussed in Section 3 permits the computation of the consistent tangent in a closed form.

4.1. Momentum balance

We consider a body B with volume Ω and surface $\partial\Omega = \partial_t\Omega \cup \partial_u\Omega$, where $\partial_t\Omega$ and $\partial_u\Omega$ are the traction and kinematic boundaries respectively with $\partial_t\Omega \cap \partial_u\Omega = 0$. In displacement based FE formulations, the momentum balance or principle of virtual work is normally fulfilled, with respect to the current configuration, in a weak form as

$$\int_\Omega (\nabla\boldsymbol{\eta} : \boldsymbol{\tau}) J^{-1}\,\mathrm{d}\Omega = \int_\Omega \boldsymbol{\eta}\cdot\mathbf{b}\,\mathrm{d}\Omega - \int_{\partial_t\Omega} \boldsymbol{\eta}\cdot\mathbf{t}\,\mathrm{d}S, \tag{48}$$

where $\boldsymbol{\tau}$ denotes the Piola–Kirchhoff stress, $\boldsymbol{\eta}$ is the virtual displacement, $\mathbf{b}$ and $\mathbf{t}$ represent the body force and surface traction, respectively. In the standard incremental approach, the stress update follows:

$$\boldsymbol{\tau} = \boldsymbol{\tau}(\mathbf{u}; \Phi_n; \Delta t), \tag{49}$$

where $\mathbf{u}$ is the incremental deformation and Φ_n the set of initial conditions. If one chooses to solve the nonlinear virtual work equation (48) by means of an iterative Newton–Raphson method, the $(I+1)$th updated stress reads

$$\boldsymbol{\tau}^{(I+1)} = \boldsymbol{\tau}^{(I)} + \delta\boldsymbol{\tau}^{(I)} \tag{50}$$

and the virtual work (Eq. 48) can be rewritten as

$$\int_\Omega (\nabla\boldsymbol{\eta} : \delta\boldsymbol{\tau}) J^{-1}\,\mathrm{d}\Omega = \int_\Omega \boldsymbol{\eta}\cdot\mathbf{b}\,\mathrm{d}\Omega - \int_{\partial_t\Omega} \boldsymbol{\eta}\cdot\mathbf{t}\,\mathrm{d}S - \int_\Omega (\nabla\boldsymbol{\eta} : \boldsymbol{\tau}^{(I)}) J^{-1}\,\mathrm{d}\Omega, \tag{51}$$

where J is the Jacobian. After lengthy but straightforward manipulations, the left-hand side can be expressed as

$$\nabla\boldsymbol{\eta} : \delta\boldsymbol{\tau} = \nabla\boldsymbol{\eta} : \mathbf{k} : \nabla(\delta\mathbf{u}) \tag{52}$$

with the so-called *consistent tangent* $\mathbf{k}$, which will be derived in Section 4.2.

4.2. The tangent modulus

Recall that the plastic flow is evaluated on $\Omega_{n+\theta}$, and consequently, the updated stress $\hat{\boldsymbol{\tau}}_{n+\theta}$ as

$$\hat{\boldsymbol{\tau}}_{n+\theta} = \hat{\boldsymbol{\tau}}^{\mathrm{tr}}_{n+\theta} - \boldsymbol{\nabla}\lambda_{n+\theta}\mathbf{r}^{\mathrm{tr}}_{n+\theta} \tag{53}$$

with the trial stress

$$\hat{\boldsymbol{\tau}}^{\mathrm{tr}}_{n+\theta} = \mathbf{f}_{n+\theta}\cdot\boldsymbol{\tau}_n\cdot\mathbf{f}^{\mathrm{T}}_{n+\theta} + \mathbf{a}_{n+\theta} : \hat{\mathbf{e}}_{n+\theta} \tag{54}$$

pushed-forward to the current configuration Ω_{n+1}, i.e.

$$\boldsymbol{\tau} = \mathbf{g}\cdot\hat{\boldsymbol{\tau}}_{n+\theta}\cdot\mathbf{g}^{\mathrm{T}} \tag{55}$$

by the relative deformation gradient $\mathbf{g}$. Differentiation of Eq. (55) leads to

$$\delta\boldsymbol{\tau} = \left[\delta\mathbf{g}\cdot\mathbf{g}^{-1}\cdot\boldsymbol{\tau} + (\delta\mathbf{g}\cdot\mathbf{g}^{-1}\cdot\boldsymbol{\tau})^{\mathrm{T}}\right] + \mathbf{g}\cdot\delta\hat{\boldsymbol{\tau}}_{n+\theta}\cdot\mathbf{g}^{\mathrm{T}}. \tag{56}$$

Using Eqs. (46) and (53) enables us to rewrite the last term of Eq. (56) in the form

$$\mathbf{g}\cdot\delta\hat{\boldsymbol{\tau}}_{n+\theta}\cdot\mathbf{g}^{\mathrm{T}} = \delta\boldsymbol{\tau}^{\mathrm{tr}} - \Delta\lambda_{n+\theta}\mathbf{q}^{\mathrm{tr}} : \delta\boldsymbol{\tau}^{\mathrm{tr}} - \hat{h}^{-1}[(\mathbf{r}^{\mathrm{tr}})\otimes(\mathbf{n}^{\mathrm{tr}} : \delta\boldsymbol{\tau}^{\mathrm{tr}})], \tag{57}$$

where

$$\mathbf{q}^{\mathrm{tr}}_{n+\theta} = \frac{\partial\mathbf{r}^{\mathrm{tr}}_{n+\theta}}{\partial\boldsymbol{\tau}^{\mathrm{tr}}_{n+\theta}}, \tag{58}$$

$$\hat{h} = h^{(i)}_{n+\theta} + 3\mu, \tag{59}$$

and the push-forward results [2]

$$\delta\boldsymbol{\tau}^{\mathrm{tr}} = \mathbf{g}\cdot\delta\hat{\boldsymbol{\tau}}^{\mathrm{tr}}_{n+\theta}\cdot\mathbf{g}^{\mathrm{T}}, \tag{60}$$

$$\mathbf{r}^{\mathrm{tr}} = \mathbf{g}\cdot\mathbf{r}^{\mathrm{tr}}_{n+\theta}\cdot\mathbf{g}^{\mathrm{T}}, \tag{61}$$

$$\mathbf{n}^{\mathrm{tr}} = \mathbf{g}^{-\mathrm{T}}\cdot\mathbf{n}^{\mathrm{tr}}_{n+\theta}\cdot\mathbf{g}^{-1}, \tag{62}$$

$$(\mathbf{q})_{ijkl} = \mathbf{g}_{im}\ \mathbf{g}_{jn}\ \mathbf{g}^{-1}_{sk}\ \mathbf{g}^{-1}_{tl}\ (\mathbf{q}_{n+\theta})_{mnst} \tag{63}$$

have been introduced, respectively. Furthermore, straightforward differentiation of Eq. (54) gives

$$\delta\hat{\boldsymbol{\tau}}^{\mathrm{tr}}_{n+\theta} = \left[\delta\mathbf{f}_{n+\theta}\cdot\boldsymbol{\tau}_n\cdot\mathbf{f}^{\mathrm{T}}_{n+\theta} + (\delta\mathbf{f}_{n+\theta}\cdot\boldsymbol{\tau}_n\cdot\mathbf{f}^{\mathrm{T}}_{n+\theta})^{\mathrm{T}}\right] + \mathbf{a}_{n+\theta} : \left[\delta\mathbf{g}^{\mathrm{T}}\cdot\mathbf{e}\cdot\mathbf{g} + (\delta\mathbf{g}^{\mathrm{T}}\cdot\mathbf{e}\cdot\mathbf{g})^{\mathrm{T}} + \mathbf{g}^{\mathrm{T}}\cdot\delta\mathbf{e}\cdot\mathbf{g}\right]. \tag{64}$$

Along with Eq. (64), using the following relationships,

$$\delta\mathbf{f}_{n+\theta}\cdot\boldsymbol{\tau}_n\cdot\mathbf{f}^{\mathrm{T}}_{n+\theta} = \theta\delta\hat{\mathbf{f}}\cdot\hat{\boldsymbol{\tau}}_n\cdot\mathbf{g}^{-\mathrm{T}}, \tag{65}$$

$$\hat{\boldsymbol{\tau}}_n = \mathbf{f}_{n+1}\cdot\boldsymbol{\tau}_n\cdot\mathbf{f}^{\mathrm{T}}_{n+1}, \tag{66}$$

$$\delta\hat{\mathbf{f}} = \delta\mathbf{f}_{n+1}\cdot\mathbf{f}^{-1}_{n+1} = \delta\mathbf{F}\cdot\mathbf{F}^{-1} = \boldsymbol{\nabla}(\delta\mathbf{u}), \tag{67}$$

$$\delta\mathbf{e} = \tfrac{1}{2}\left[\mathbf{b}\cdot\delta\hat{\mathbf{f}} + (\mathbf{b}\cdot\delta\hat{\mathbf{f}})^{\mathrm{T}}\right], \qquad \mathbf{b} = (\mathbf{f}_{n+1}\cdot\mathbf{f}^{\mathrm{T}}_{n+1})^{-1}, \tag{68}$$

$$\delta\hat{\mathbf{g}} = \delta\mathbf{g}\cdot\mathbf{g}^{-1} = \mathbf{i}\cdot\delta\hat{\mathbf{f}}, \qquad \mathbf{i} = [\mathbf{I} - \theta\mathbf{g}], \tag{69}$$

[2] Note that $\boldsymbol{\tau}$ and $\mathbf{r}$ are contravariant tensors, $\mathbf{n}$ is a covariant tensor and $\mathbf{q}$ is a mixed contravariant–covariant tensor.

$$\mathbf{g}\cdot\left[\mathbf{a}:(\mathbf{g}^{\mathrm{T}}\cdot\mathbf{e}\cdot\mathbf{g})\right]\cdot\mathbf{g}^{\mathrm{T}}=\hat{\mathbf{a}}:\mathbf{e}, \tag{70}$$

Eq. (60) yields

$$\delta\boldsymbol{\tau}^{\mathrm{tr}}=\theta\left[\mathbf{g}\cdot\delta\hat{\mathbf{f}}\cdot\hat{\boldsymbol{\tau}}_n+(\mathbf{g}\cdot\delta\hat{\mathbf{f}}\cdot\hat{\boldsymbol{\tau}}_n)^{\mathrm{T}}\right]+\hat{\mathbf{a}}:\left[\mathbf{e}\cdot\delta\hat{\mathbf{g}}+\delta\hat{\mathbf{g}}^{\mathrm{T}}\cdot\mathbf{e}+\delta\mathbf{e}\right]. \tag{71}$$

By applying tensor algebra in Eq. (71), one obtains

$$\delta\boldsymbol{\tau}^{\mathrm{tr}}=\mathbf{k}^{\mathrm{tr}}:\nabla(\delta\mathbf{u}), \tag{72}$$

where

$$k^{\mathrm{tr}}_{ijkl}=\theta[g_{ik}(\hat{\tau}_n)_{lj}+g_{jk}(\hat{\tau}_n)_{li}]+\hat{a}_{ijab}[\delta_{la}e_{cb}i_{ck}+\delta_{lb}e_{ca}i_{ck}]+\hat{a}_{ijab}\left[\tfrac{1}{2}(b_{ak}\delta_{bl}+b_{kb}\delta_{al})\right], \tag{73}$$

$$\hat{a}_{ijab}=g_{ie}g_{jf}g_{ag}g_{bh}(a_{n+\theta})_{efgh}. \tag{74}$$

Substitution of Eq. (71) into Eq. (56) leads to

$$\mathbf{k}=\mathbf{k}^{\mathrm{tr}}+\mathbf{k}^{\mathrm{c}}-\mathbf{k}^{\mathrm{p}}, \tag{75}$$

where

$$k^{\mathrm{c}}_{ijkl}=i_{ik}\tau_{lj}+i_{jk}\tau_{li} \tag{76}$$

$$\mathbf{k}^{\mathrm{p}}=\hat{h}^{-1}\left[(\mathbf{r}^{\mathrm{tr}})\otimes(\mathbf{n}^{\mathrm{tr}}:\mathbf{k}^{\mathrm{tr}})\right]+\Delta\lambda_{n+\theta}\mathbf{q}^{\mathrm{tr}}:\mathbf{k}^{\mathrm{tr}}. \tag{77}$$

In general, the tangent stiffness (Eq. 75) lacks the symmetry, and the formulation process needs many tensor multiplications and inverse calculations. Furthermore, the stability of the return mapping algorithm, in general, requires a large value of interpolation parameter θ, especially when larger strain increments are considered. If we take $\theta=1$, the relative deformation tensor $\mathbf{g}$ becomes the identity tensor, and therefore, the tensor $\mathbf{i}$ vanishes from Eq. (75). Rewriting Eq. (75), one obtains the consistent tangent

$$\mathbf{k}=\mathbf{k}^{\mathrm{e}}+\mathbf{k}^{\mathrm{g}}-\mathbf{k}^{\mathrm{p}}, \tag{78}$$

where

$$k^{\mathrm{e}}_{ijkl}=\bar{\lambda}\delta_{ij}b_{kl}+\mu[b_{ik}\delta_{jl}+b_{jk}\delta_{il}], \tag{79}$$

$$k^{\mathrm{g}}_{ijkl}=[\delta_{ik}(\hat{\tau}_n)_{lj}+\delta_{jk}(\hat{\tau}_n)_{li}], \tag{80}$$

$$\mathbf{k}^{\mathrm{p}}=\frac{4\mu}{h+3\mu}\left[\mathbf{n}^{\mathrm{tr}}\otimes(\mathbf{n}^{\mathrm{tr}}\cdot\hat{\boldsymbol{\tau}}_n+\mu\mathbf{b}\cdot\mathbf{n}^{\mathrm{tr}})\right]+\frac{2\mu}{\sqrt{3J_2}}\Delta\lambda_{n+\theta}\left[\mathbf{k}^{\mathrm{p1}}-\mathbf{k}^{\mathrm{p2}}\right] \tag{81}$$

with

$$(\mathbf{k}^{\mathrm{p1}})_{ijkl}=\tfrac{3}{2}[\delta_{ik}(\hat{\tau}_n)_{lj}+\delta_{jk}(\hat{\tau}_n)_{li}]+\tfrac{3}{2}\mu[b_{ik}\delta_{jl}+b_{jk}\delta_{il}], \tag{82}$$

$$\mathbf{k}^{\mathrm{p2}}=\mathbf{I}\otimes(\hat{\boldsymbol{\tau}}_n+\mu\mathbf{b})+\mathbf{n}^{\mathrm{tr}}\otimes(\mathbf{n}^{\mathrm{tr}}\cdot\hat{\boldsymbol{\tau}}_n+\mu\mathbf{b}\cdot\mathbf{n}^{\mathrm{tr}}). \tag{83}$$

5. Numerical examples

To demonstrate the performance of the consistency viscoplastic model in conjunction with the finite strain numerical scheme discussed before, numerical examples are presented in this chapter. All numerical

simulations are performed by using the Newton–Raphson iteration procedure with a fully backward Euler integration scheme.

5.1. Strip in tension-shear banding

First, the influence of geometrical nonlinearity in the evolution of the shear band is investigated. It is well known that the onset of strain softening, in the classical small strain theory, will result in the mathematical ill posedness of the field equations. No length scale is involved in the evolution of the shear band, and therefore, the localization zone stays confined to the size of one element. Consequently, a finer element size results in a smaller shear band thickness with higher peak strains. To investigate the influence of geometrical nonlinearities in the evolution of the shear band, the simulation of a strip in tension as shown in Fig. 4 is carried out. The strip is constrained at the bottom, while a constant velocity $v = 20$ mm/s is imposed at the top. Von Mises plasticity is used with the initial yield stress $\bar{\sigma}_0 = 20$ N/mm^2. Strain softening is assumed via $h = -0.025E$ with Young's modulus $E = 20\,000$ N/mm^2 and Poisson's ratio $\nu = 0.3$. Two meshes (mesh 1: 10×20, mesh 2: 20×40) have been used with a four-noded quadrilateral plane-strain element. To avoid a homogeneous solution, we slightly increase the width of the specimen towards the top, so that the shear band will be initiated at the bottom left and develops with an inclination angle $\Theta \approx 45^\circ$, which is the analytical solution for a 2D infinite medium under plane-strain condition for a small strain analysis (Sluys, 1992). In Fig. 5, the displacement patterns for both meshes have been plotted. We observe that the width of the shear band is determined by the element size for a standard strain softening model. Deformation is localized along a line of integration points. Mesh dependence is also obvious from the load–deformation curve. When the mesh is refined, the dissipated energy is decreasing. So, the inclusion of geometrical nonlinearity in the description of the strain softening material cannot solve this discretization dependence.

In order to solve the mesh-sensitivity problem, viscous terms can be introduced to keep the field equations well posed. Needleman (1988), Loret and Prevost (1990) and Sluys (1992) have shown that the material rate dependence introduces a length scale effect into the initial value problem, even though the constitutive equations do not explicitly contain a parameter with the dimension of length. Sluys (1992) has demonstrated that this viscous length scale effect can be related to the spatial attenuation of waves that have real wave speeds in the softening regime. Wang et al. (1996) found an expression for the internal length scale and examined the influence of a material imperfection on shear band formation.

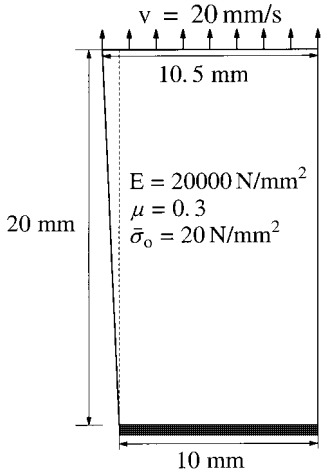

Fig. 4. Strip in tension.

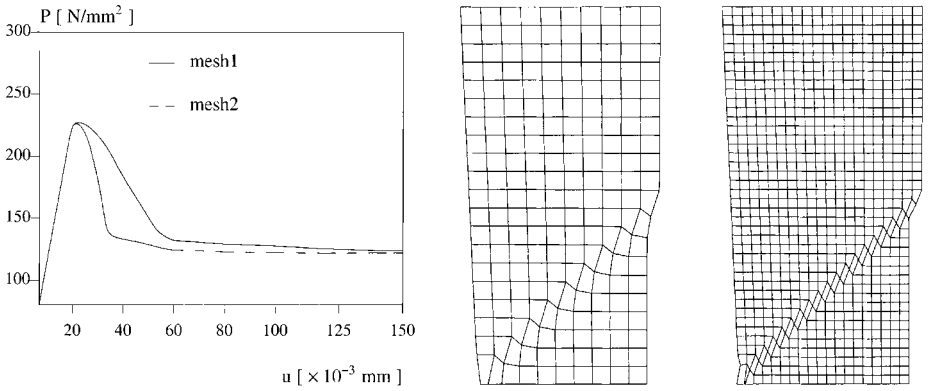

Fig. 5. Mesh-dependent results with a standard strain-softening model. left: load–deformation curve, right: displacement patterns.

It should be emphasized that the introduction of rate dependence has a regularization effect not only in the dynamic case but also in the quasi-static case as we present here (Sluys and Wang, 1998). We use the data set from the former calculation, but additionally introduce a linear viscosity term in the yield function as mentioned in Section 3.1. Thus,

$$\bar{\sigma} = \bar{\sigma}_0 + h\kappa + s\dot{\kappa},$$

where κ is the equivalent plastic strain and s the viscosity parameter. In Fig. 6, the displacement patterns and the load–deformation curve have been plotted ($s = 0.4$ Ns/mm^2). By comparison with the results of Fig. 5, one observes that the shear band has a finite width which is independent of the finite element size.

Next, the influence of viscosity in case of strain hardening is investigated. With a nearly perfect plasticity model ($h = 10^{-6} \times E$), one can obtain mesh objective results without viscosity contribution ($s = 0$, Fig. 7), because the field equations remain well posed in case of strain hardening. If we apply a small viscosity ($s = 0.02$ Ns/mm^2), the same results are obtained (Fig. 8), however, one observes a faster convergence rate. The average number of global iterations for consistency viscoplastic model is 3.6, while the standard model takes 6.1 iterations. From a numerical point of view, the viscosity *helps* to constrain the deformation process at the initial state of plastification while the local strain rate is very high. When the shear band is fully developed, the influence of viscosity decreases. Therefore, the prediction of the deformation process is more accurate and robust with a consistency viscoplastic tangent stiffness.

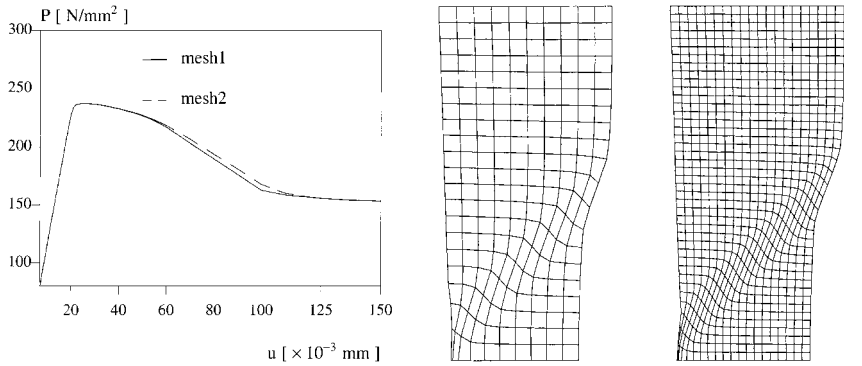

Fig. 6. Mesh objective results with the consistency viscoplastic model. left: load–deformation curve, right: displacement patterns.

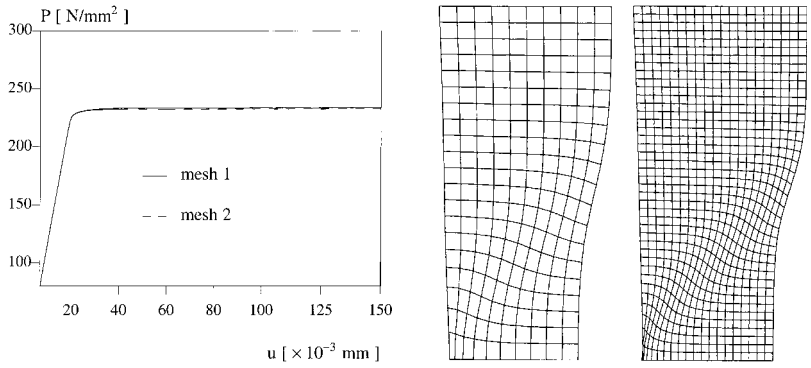

Fig. 7. Mesh objective results with strain hardening. left: load–deformation curve, right: displacement patterns.

Finally, to demonstrate the applicability of the computational procedures at finite strain, we continue to stretch the strip until the whole bar is strained up to 50% deformation. In Fig. 9 the contours of the equivalent plastic strain are plotted at different stages. First, we observe the development of the shear band and in a later stage a necking failure mode evolves. Quadratic rate of convergence remains during the complete deformation process.

5.2. Thin sheet tensile test-necking

Experiments on thin aluminum sheet have been carried out at CEMEF. The thin sheet is clamped at the left end while a constant velocity $v = 10$ mm/min is imposed at the right (Fig. 10). Von Mises plasticity is used with an initial yield stress $\bar{\sigma}_0 = 135$ Mpa. After the initiation of (visco)plasticity, plastic flow is described by a power law

$$\bar{\sigma} = a + b(c + \kappa)^d \tag{84}$$

with the material constants $a = 25$ Mpa, $b = 466$ Mpa, $c = 0.003$ and $d = 0.293$. Young's modulus $E = 70$ GPa and Poisson's ratio $v = 0.3$. A three-noded triangular plane-stress element has been used. In Fig. 11, the load–deformation curves have been plotted. With the small strain algorithm, no global softening behavior is observed. With the contribution of geometrical nonlinearity, however, one observes the global softening at around 20% deformation, even though, locally, the material shows hardening behavior (Eq. (84)). From Figs. 11 and 12, one observes that before the peak load, the numerical simulation matches the experimental data well and we have objective results for different meshes (mesh 1 with 316 elements, mesh 2 with 1138 elements). However, it is to be noted that as soon as the peak load is passed, mesh-dependent results are observed. If we introduce the viscosity term in the numerical simulations, we can bypass the peak load without loss of objectivity (Fig. 13). However, when necking takes place, the mesh dependence reappears despite the use of viscoplastic regularization. The reason for this mesh-dependent result is probably the dramatic change in geometry in the necking zone. From Fig. 13, it can be seen that with increasing viscosity, the moment at which the results become mesh dependent is extended.

6. Conclusions

Within the framework of additive plasticity, an objective stress update algorithm has been proposed. The procedure is implemented in such way that the extension from a standard small strain FE code to the finite

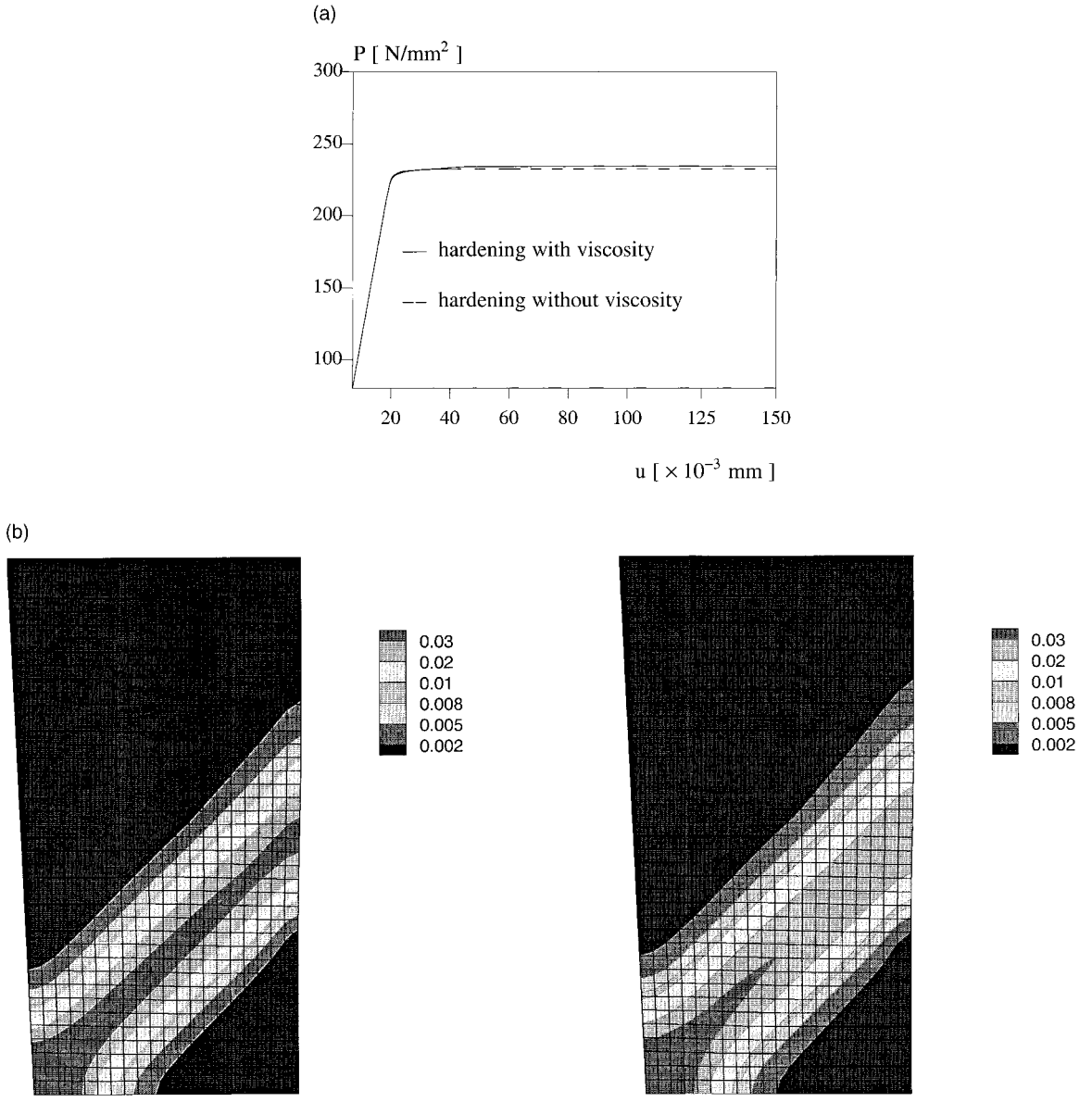

Fig. 8. The influence of viscosity in the case of strain hardening. (a) load–deformation curve, middle and (b) contour plot of the equivalent plastic strain without and with viscosity.

strain range is straightforward, and objectivity can be retained for any choice of the intermediate configuration. The additional computational cost only includes some geometrical manipulations. In conjunction with the Newton–Raphson iteration method, a closed-form solution of the consistent tangent is derived by direct linearization of the stress update algorithm. Numerical examples show a quadratic rate of convergence with the proposed viscoplastic model. It has been found that the viscosity not only has the regularization effect on the description of the localization problem, but also helps to improve the convergence rate by constraining the deformation process at the initial state of plastification, which is the crucial

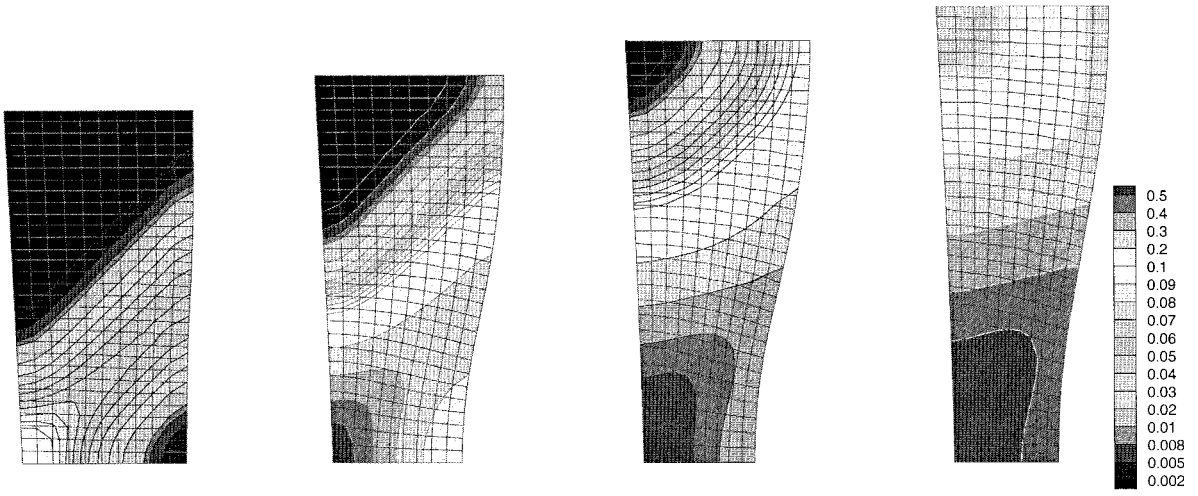

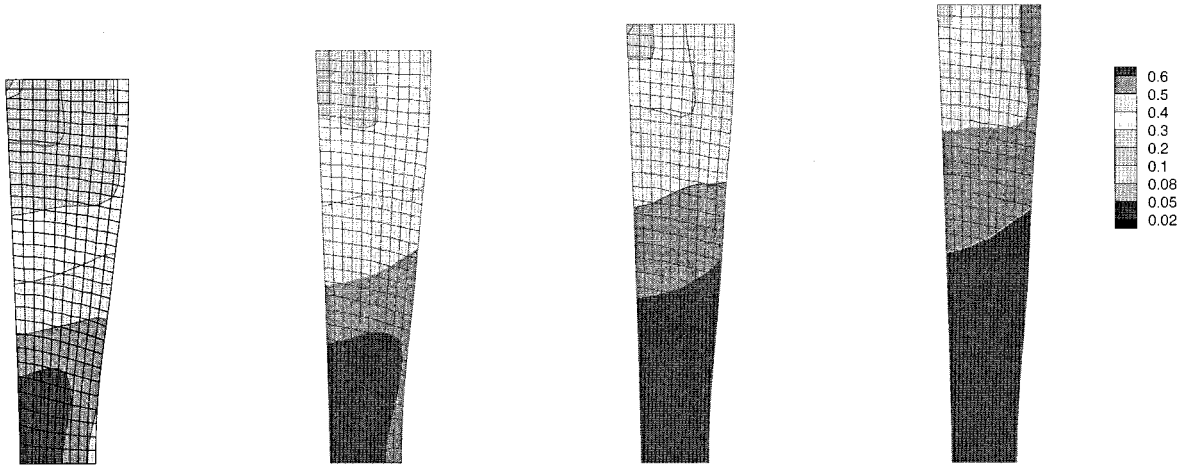

Fig. 9. Stretch test: contours of the equivalent plastic strain at various stages.

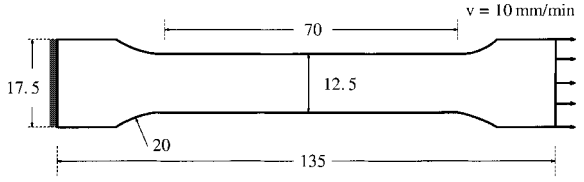

Fig. 10. Thin sheet tensile test.

restriction of the time step in the numerical simulation of the localization problem. The analysis of a tensile test first shows a shear band with a finite thickness independent of the finite element size. At large deformation, the shear band pattern transforms into a necking failure mode. As a second example, a thin

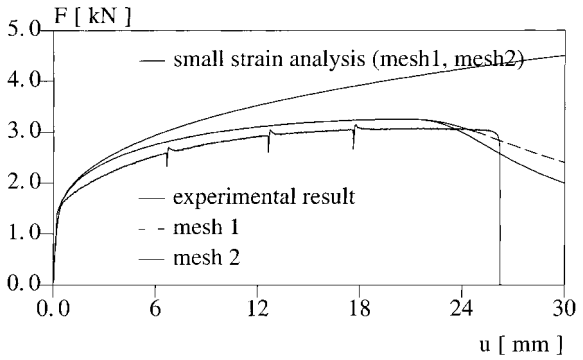

Fig. 11. Load–displacement curve.

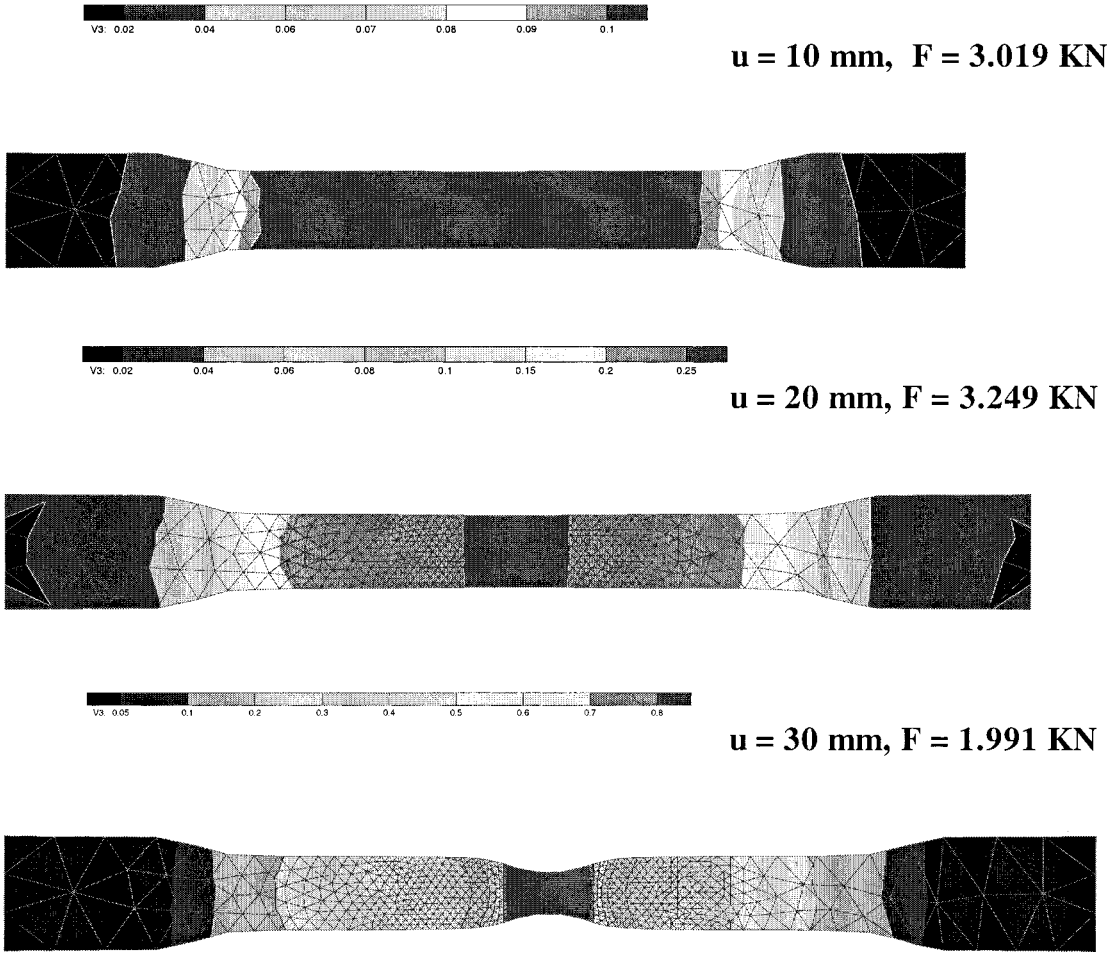

Fig. 12. Contour plots of equivalent plastic strain.

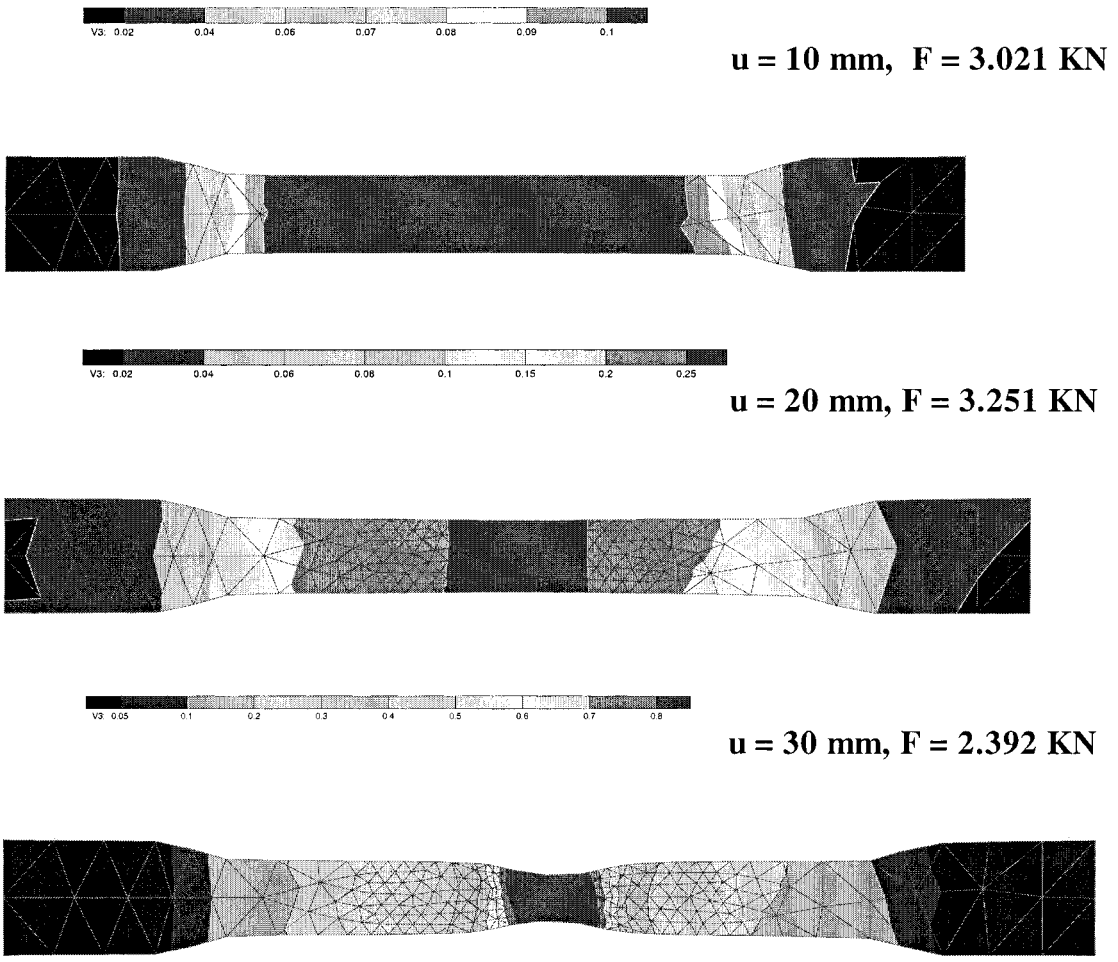

Fig. 12. (*continued*)

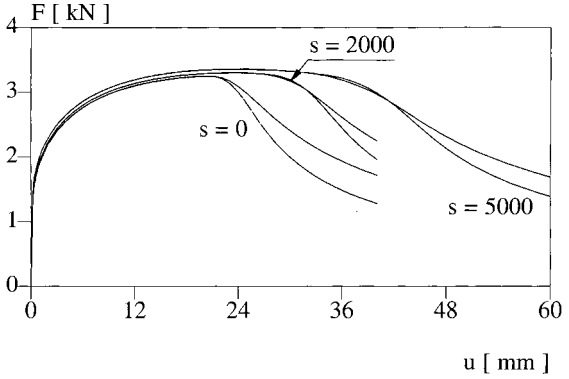

Fig. 13. Load–displacement curve.

sheet tensile test is analyzed. A necking failure mode leads to global softening even though, locally, the material is still hardening. Although viscoplastic regularisation is used, the results still show a mesh dependence for deformations over 40%.

Acknowledgements

Financial support from the European Community through grant BE-97-4517 is gratefully acknowledged. The authors thank R. Knockaert (CEMEF) for providing the experimental data for the thin sheet tensile test.

Appendix A

A.1. Implicit stress-update algorithm at finite strain

(1) Given $[\boldsymbol{\tau}_n, \lambda_n]$ and the increment displacement $\mathbf{u}$, compute the relative deformation gradients as

$$\mathbf{f} = \mathbf{I} + \nabla_n \mathbf{u},$$

$$\mathbf{f}_{n+\theta} = \mathbf{I} + \theta \nabla_n \mathbf{u},$$

$$\mathbf{g} = \mathbf{f} \cdot \mathbf{f}_{n+\theta}^{-1}.$$

(2) Compute the relative (incremental) Eulerian strain and the initial stress at the intermediate configuration as

$$\mathbf{e} = \tfrac{1}{2}[\mathbf{I} - (\mathbf{f} \cdot \mathbf{f}^{\mathrm{T}})^{-1}],$$

$$\hat{\mathbf{e}}_{n+\theta} = \mathbf{g}^{\mathrm{T}} \cdot \mathbf{e} \cdot \mathbf{g},$$

$$\hat{\boldsymbol{\tau}}_n = \mathbf{f}_{n+\theta} \cdot \boldsymbol{\tau}_n \cdot \mathbf{f}_{n+\theta}^{\mathrm{T}}.$$

(3) Small-strain return mapping algorithm.

(4) Push forward to the current configuration

$$\boldsymbol{\tau}_{n+1} = \mathbf{g} \cdot \hat{\boldsymbol{\tau}}_{n+\theta} \cdot \mathbf{g}^{\mathrm{T}}.$$

A.2. Small-strain stress-update algorithm for the J_2 flow theory

(1) Given $[\hat{\boldsymbol{\tau}}_n, \lambda_n]$ and the incremental strain $\hat{\mathbf{e}}_{n+\theta}$, compute trial stress as

$$\hat{\boldsymbol{\tau}}_{n+\theta}^{\mathrm{tr}} = \hat{\boldsymbol{\tau}}_n + \mathbf{a}_{n+\theta} : \hat{\mathbf{e}}_{n+\theta},$$
$$\hat{\mathbf{s}}_{n+\theta}^{\mathrm{tr}} = \hat{\boldsymbol{\tau}}_{n+\theta}^{\mathrm{tr}} - \tfrac{1}{3}\mathrm{tr}(\hat{\boldsymbol{\tau}}_{n+\theta}^{\mathrm{tr}})\mathbf{I},$$
$$\phi_{n+\theta}^{\mathrm{tr}} = \sqrt{3J_2(\hat{\boldsymbol{\tau}}_{n+\theta}^{\mathrm{tr}})} - \hat{\sigma}(\lambda_n),$$
$$\mathbf{n}_{n+\theta}^{\mathrm{tr}} = \sqrt{\frac{3}{2}}\frac{\hat{\mathbf{s}}_{n+\theta}^{\mathrm{tr}}}{|\hat{\mathbf{s}}_{n+\theta}^{\mathrm{tr}}|}.$$

(2) Standard return-mapping algorithm.

if $\phi^{\mathrm{tr}}_{n+\theta} < 0$ then

$\hat{\boldsymbol{\tau}}_{n+\theta} = \hat{\boldsymbol{\tau}}^{\mathrm{tr}}_{n+\theta}$

$\lambda_{n+1} = \lambda_n$

else

$\Delta\lambda^{(i+1)} = \Delta\lambda^{(i)} + \phi^{(i)}_{n+\theta}(3\mu + h^{(i)})^{-1}$

$\hat{\boldsymbol{\tau}}_{n+\theta} = \hat{\boldsymbol{\tau}}^{\mathrm{tr}}_{n+\theta} - 2\mu\Delta\lambda^{(i+1)}\mathbf{n}^{\mathrm{tr}}_{n+\theta}$

$\lambda_{n+1} = \lambda_n + \Delta\lambda^{(i+1)}, \quad \dot{\lambda}_{n+1} = \Delta\lambda^{(i+1)}/\Delta t$

until $\phi_{n+\theta}(\hat{\boldsymbol{\tau}}_{n+\theta},\ \lambda_{n+1},\ \dot{\lambda}_{n+1}) < \delta$

end if

References

Cuitino, A., Ortiz, M.A., 1992. A material-independent method for extending stress update algorithms from small-strain plasticity to finite plasticity with multiplicative kinematics. Engng. Comp. 9, 437–451.

Hughes, T.J.R., 1983. Analysis of transient algorithms with particular emphasis in stability behavior. Comp. Meth. for Transient Analysis, North-Holland, Amsterdam.

Loret, B., Prevost, J.H., 1990. Dynamic strain localization in elasto-(visco-)plastic solids, Part 1: General formulation and one-dimensional examples. Comp. Meth. Appl. Mech. Engng. 83, 247–273.

Malvern, L.E., 1969. Introduction to the mechanics of a continuous medium. Prentice-Hall, Englewood Cliffs, New Jersey.

Needleman, A., 1988. Material rate dependence and mesh sensitivity on localisation problems. Comp. Meth. Appl. Mech. Engng. 67, 69–86.

Rodriguez-Ferran, A., Pegon, P., Huerta, A., 1997. Two stress update algorithms for large strains: Accuracy analysis and numerical implementation. Int. J. Num. Meth. Engng. 40, 4363–4404.

Simo, J.C., Marsden, J.E., 1984. On the rotated stress tensor and the material version of the Doyle–Ericksen formula. Archive Rat. Mech. Anal. 86, 213–321.

Simo, J.C., Ortiz, M.A., 1985. A unified approach to the finite deformation elastoplastic analysis based on the use of hyperelastic constitutive equations. Comp. Meth. Appl. Mech. Engng. 49, 221–245.

Sluys, L.J., 1992. Wave propagation, localisation and dispersion in softening solids, Ph.D. Thesis, Delft University of Technology, Netherlands.

Sluys, L.J., Wang, W.M., 1998. Macroscopic modelling of stationary and propagative instabilities. In: de Borst, R., van der Giessen, E., (Eds.), Material Instabilities in Solids, Wiley, New York, pp. 489–505.

Wang, W.M., Sluys, L.J., de Borst, R., 1996. Interaction between material length scale and imperfection size for localisation in viscoplastic media. European J. Mech. A/Solid 15 (3), 447–464.

Wang, W.M., Sluys, L.J., de Borst, R., 1997. Viscoplasticity for instabilities due to strain softening and strain-rate softening. Int. J. Num. Meth. Engng. 40, 3839–3864.